



1 Relations of the low-level extra-tropical cyclones in the Southeast Pacific and South
2 Atlantic to the Atlantic multi-decadal oscillation

3
4 Mary Toshie Kayano¹, Marcelo Barbio Rosa¹, Vadlamudi Brahamananda Rao^{1,2}, Rita
5 Valéria Andreoli³ and Rodrigo Augusto Ferreira de Souza³

6
7 ⁽¹⁾ Instituto Nacional de Pesquisas Espaciais, Centro de Previsão de Tempo e Estudos
8 Climáticos, São José dos Campos, SP, Brazil

9 ⁽²⁾ Andhra University, Department of Meteorology and Oceanography, India

10 ⁽³⁾ Universidade do Estado do Amazonas, Escola Superior de Tecnologia, Manaus, AM,
11 Brazil

12
13 Corresponding author: Mary Toshie Kayano

14 mary.kayano@inpe.br

15

ABSTRACT

16
17
18
19
20
21
22
23
24
25
26
27
28
29
30
31
32
33
34
35
36
37

The relations of the low-level extra-tropical cyclones in the southeastern Pacific and South Atlantic with the sea surface temperature (SST) anomalies associated with the Atlantic multi-decadal oscillation (AMO) during the summer and winter of the 1979-1993 (cold AMO- CAMO) and 2003-2017 (warm AMO - WAMO) are analyzed. During both seasons and in both AMO phases, the cyclone trajectories defined by cyclone local counts exceeding 10 events per grid box occur approximately in the areas with the AMO-related positive SST anomalies. The cyclone densities in most latitudes during both seasons are higher in the CAMO than in the WAMO. Thus, the cyclone density in the study domain presents a reduction trend during the 1979-2017 period. The large-scale northward SST anomalous gradients between the bands north and south of 40°S increase the long wave baroclinicity in the mid-latitudes in the WAMO, and the southward SST anomalous gradients decrease it in the CAMO. Consequently, the short wave baroclinicity is higher in the WAMO than in CAMO in the southeastern Pacific mid-latitudes. Thus, the cyclones are more energetic in the WAMO than in the CAMO. In the South Atlantic region off the Argentinean coast, both the barotropic and baroclinic conversion terms are positive indicating increase of the kinetic energy of the short waves. The low-level cyclones in the southeastern Pacific and South Atlantic are modulated by the AMO. As far as we know, the relation of the SH low-level extra-tropical cyclones to the AMO documented here was not studied before.

38 **1. Introduction**

39

40 Migratory cyclones are important parts of the general circulation in transporting
41 heat, momentum and moisture between the equator and the poles (Peixoto and Oort 1992),
42 and in driving weather and climate. Using automatic tracking schemes, several authors
43 analyzed the climatological features of the Southern Hemisphere (SH) mean sea level
44 extra-tropical cyclones, their trends and variability (Jones and Simmonds 1993; Sinclair
45 1994; 1995; 1997; Simmonds and Keay 2000a; Mendes et al. 2009; Eichler and
46 Gottschalck 2013; Neu et al. 2013; Wang et al. 2013; Reboita et al. 2015; Grieger et al.
47 2018). These studies indicated that the cyclone climatological features depend on the
48 dataset, period of analysis and tracking method used.

49 Wang et al. (2013) identified these systems in the SH using the National Oceanic
50 and Atmospheric Administration (NOAA)-Twentieth Century Reanalysis (NOAA-
51 20CR) data during the 1871-2010 period, and showed trends in the cyclone activity index
52 that vary with the seasons and regions. During winter, they found increases in this index
53 in the circumpolar latitudes of the South Atlantic-Indian Ocean, and decreases in southern
54 Australia, in the circumpolar latitudes of the South Pacific and in the region to the
55 southeast of South America. During summer, they registered increases in the cyclone
56 activity index in the South Atlantic, eastern South Pacific and around the circumpolar
57 latitudes, and decreases in the Indian Ocean and western South Pacific. Neu et al. (2013)
58 showed that different algorithms give similar patterns of the number of cyclones in the
59 extratropics of both hemispheres in particular the strong events. Grieger et al. (2018)
60 confirm this result for the SH events. Nevertheless, both studies recommended caution
61 with respect to the total cyclone counts when only one method is used.

62 Befort et al. (2016) compared the long-term trends of extratropical cyclones
63 during the 1901-1930, 1931-1960 and 1961-1990 periods using two reanalysis datasets:
64 NOAA-20CR and European Centre for Medium-Range Weather Forecasts (ECMWF)
65 Twentieth Century Reanalysis (ERA-20C). In the SH, they registered large differences
66 between the datasets. In the NOAA-20CR, they found an increase in the cyclone activity
67 in all regions, except the Pacific by 1970 and a decrease afterwards, and an increase in
68 the number of extreme cyclones from 1920 to 2000. In the ERA-20C, they found an
69 increase in the cyclone activity over the twentieth century, and a local maximum in the
70 number of extreme cyclones by 1940, and two local minima, one by the beginning of the
71 twentieth century and the other by 1960. Another aspect raised by Schneider and Fogt
72 (2018) concerns the spurious pressure decrease trends in the 60-90°S band during the
73 1905-2010 period in the NOAA-20CR, ERA-20C and ECMWF's coupled Ocean-
74 Atmosphere Twentieth Century Reanalysis (CERA-20C), which reflect the number of
75 assimilated observations. All these results indicate that the trends in the cyclone activity
76 in the SH should be taken with care.

77 On the other hand, Simmonds and Keay (2000a) documented a variability of the
78 SH extra-tropical cyclones using the 6 hourly National Centers for Environmental
79 Prediction-National Center for Atmospheric Research (NCEP-NCAR) reanalysis during
80 the 1958-1997 period. They found an increase in the annual average number of cyclones
81 in the entire SH and 30-70°S bands from the beginning of the period up to a maximum
82 that occurred, respectively in the 1972 and 1970 years. They associated the decrease trend
83 after these years with the SH warming, and argued that the low frequency variability of
84 the number of these systems might be related to the decadal and multi-decadal sea surface
85 temperature (SST) variability in the SH. In this context, several authors registered a
86 decadal variability of the SST in the outflow regions of the western boundary currents in

87 the SH, which coincide with those dominated by the mid-latitude westerlies (Parker et al.
88 1994; Venegas et al. 1996; 1998; Reason 2000). Using a general atmospheric circulation
89 model, Reason and Murray (2001) provided indications that the SH extratropical cyclones
90 are affected by the underlying SST variations in a decadal time scale. With a warming
91 forcing over the entire SH mid-latitudes and 21-year integrations, they obtained a large-
92 scale trough in the mid-latitudes and a ridge in the higher latitudes, which lead to increases
93 in the baroclinicity and the cyclone density in the 40-55°S band and decreases to the south
94 of this band.

95 Reason and Murray's (2001) work concerned the SST decadal variability in the
96 SH mid-latitudes noted previously in a number of papers (Venegas et al. 1996; 1998).
97 However, persistent SST anomalies in the extra-tropical Southern Oceans also occur in
98 longer time scales. One phenomenon that might cause such anomalies is the well-known
99 large-scale multi-decadal climate variability mode whose main action center is located in
100 the North Atlantic, the so-called Atlantic Multi-decadal Oscillation (AMO) (Enfield et al.
101 2001; Kerr 2000, among others). Schlesinger and Ramankutty (1994) identified the AMO
102 signal as a 65-80-year period oscillation in the spectrum analysis of the surface air
103 temperature time series of the North Atlantic. Later, several authors showed that the
104 AMO-related SST anomaly pattern features the same sign anomalies in most of the North
105 Atlantic (Enfield and Mestas-Núñez 1999; Enfield et al. 2001; Goldenberg et al. 2001;
106 Mestas-Núñez and Enfield 2001), and opposite sign SST anomalies in large extensions
107 of the extra-tropical southern oceans (Folland et al. 1999; Timmermann et al. 2007). The
108 AMO is related to thermohaline circulation changes varying from decadal to multidecadal
109 time scales (Kerr 2000; Delworth and Mann 2000; Knight et al. 2006), with a clear
110 signature in the SST field in the Weddell Sea, as shown in a modeling study by Crowley
111 and Kim (1993). The warm AMO (WAMO) phase features anomalously warmed North

112 Atlantic and anomalously cooled South Atlantic and South Pacific Oceans, and the cold
113 AMO (CAMO), an almost reversed sign SST anomaly pattern. The AMO-related SST
114 anomaly pattern in the extra-tropical oceans might impact the baroclinicity and
115 consequently the low-level extra-tropical cyclones. Studies regarding this issue have been
116 done for the Northern Hemisphere systems (Gómara et al. 2016; Varino et al. 2018). As
117 far as we know, similar studies for the SH low-level extra-tropical cyclones have not yet
118 been done.

119 Another important aspect that has received little attention concerns the energetics
120 of SH low-level extra-tropical cyclones, in particular in the southeastern Pacific and South
121 Atlantic region. Few studies can be found on this issue in the literature in particular
122 concerning the South American neighboring regions (Orlanski and Katzfey 1991; Gan
123 and Rao 1999; Pinto and Rocha 2011; Rosa et al. 2013). So, this aspect is dealt in the
124 present analysis.

125 Here, the SH low-level extra-tropical cyclones during two AMO phases are
126 investigated by focusing on the number of cyclones per grid box and the related energetics
127 in the southeastern Pacific and South Atlantic regions. Analyses are done for two periods
128 with 15 years each: 1979-1993 for the CAMO phase, and 2003-2017, for the WAMO
129 phase, which do not include years when the AMO phase changed. The following section
130 presents a brief description of the data and methodology. Section 3 presents the
131 differences between the two selected periods for the low-level extra-tropical cyclones
132 concerning their trajectories and the associated patterns of the kinetic energy, available
133 potential energy and the barotropic and baroclinic conversion terms of the Lorenz energy
134 cycle. Conclusions are drawn in Section 4.

135

136 **2. Data and Methodology**

137

138 Thirty nine years (1979-2017) of 6 hourly air temperature (T), vertical velocity
139 in pressure coordinate (ω), geopotential height (Z), and zonal and meridional winds (u
140 and v , respectively) data from the NCEP-DOE Reanalysis-II (2018) dataset developed by
141 Kanamitsu et al. (2002) were used here. These data at a 2.5° horizontal resolution grid
142 and at standard levels from 1000 hPa to 25 hPa, were obtained over the SH to the south
143 of 20°S .

144 The SST dataset used here is independent from those used in the NCEP-DOE
145 Reanalysis-II, which are: global ice and SST from the Hadley Centre for the period from
146 December 1978 to November 1981 and since then the optimum interpolation SST. Here,
147 we used the monthly mean SST data in a 2° horizontal grid from the extended
148 reconstructed SST (NOAA/ERSST, 2018) version V5 data for the 1870-2017 period
149 (Huang *et al.*, 2015). These data were used to support the hypothesis that the SST anomaly
150 patterns for the two selected periods contain the AMO-related features. In this case, first
151 the time series in each grid point is de-trended in order to remove the climate change
152 effects. The monthly anomalies were based on the 1979-2017 period. Then, the summer
153 and winter SST anomaly patterns of the 1979-1993 and 2003-2017 periods were obtained.

154 The AMO index was obtained from the NOAA web site (NOAA/AMO, 2019). In
155 addition, the Pacific Decadal Oscillation (PDO) index was extracted from the Joint
156 Institute for the Study of the Atmosphere and Ocean (JISAO) web site (JISAO/PDO,
157 2019).

158 The Lorenz energy cycle of the high frequency disturbances was analyzed.
159 Similar to Blackmon's (1976) analysis, we used a Fourier harmonic longitudinal
160 decomposition over the entire globe instead of time filtering, and the first five modes
161 added to the zonal means were considered as the long waves (l), and the complementary

162 modes, the short waves (h). The energy cycle equations after Gan and Rao (1999) are
 163 given by:

$$164 \quad P_h = g^{-1} \int \frac{T_h^2}{2\sigma} dp \quad (1)$$

165

$$166 \quad K_h = g^{-1} \int \frac{u_h^2 + v_h^2}{2} dp \quad (2)$$

167

$$168 \quad \frac{\partial K_h}{\partial t} = P_h K_h + K_l K_h + R K_h \quad (3)$$

169

$$170 \quad \frac{\partial P_h}{\partial t} = P_l P_h - P_h K_h + R P_h \quad (4)$$

171

$$172 \quad P_l P_h = -g^{-1} \int \sigma^{-1} \left(u_h T_h \frac{\partial T_l}{\partial x} + v_h T_h \frac{\partial T_l}{\partial y} \right) dp \quad (5)$$

173

$$174 \quad K_l K_h = -g^{-1} \int \left(u_h u_h \frac{\partial u_l}{\partial x} + u_h v_h \frac{\partial u_l}{\partial y} + v_h u_h \frac{\partial v_l}{\partial x} + v_h v_h \frac{\partial v_l}{\partial y} \right) dp \quad (6)$$

175

$$176 \quad P_h K_h = -g^{-1} \int \frac{R}{p} \omega_h T_h dp \quad (7)$$

177 where, the subscripts h and l refer, respectively, to the short and long waves, P and K are
 178 the available potential energy and kinetic energy. The other parameters are: g , the
 179 gravitational acceleration (m s^{-2}); T , the air temperature (K); u and v , the zonal and
 180 meridional wind components (m s^{-1}); ω , the vertical velocity in pressure coordinate (hPa
 181 s^{-1}); R the ideal gas constant; and, $\sigma = \left(\frac{T_l}{c_p} - \frac{p}{R} \frac{\partial T_l}{\partial p} \right)$ the static stability parameter. For the
 182 baroclinic conversion term in this cycle, the available potential energy of the long waves
 183 is converted into the potential energy of the short waves ($P_l P_h$), which, in turn, is

184 converted into the kinetic energy of short waves ($P_h K_h$). Therefore, we analyzed here the
185 summation ($P_l P_h + P_h K_h$), which is called baroclinic conversion term. For the barotropic
186 conversion term ($K_l K_h$), a positive value represents the conversion of the kinetic energy
187 of the long waves into the kinetic energy of the short waves. Since the interest here is the
188 low-level extra-tropical cyclones, only these two energy conversion terms were analyzed.

189 Using the horizontal winds, the relative vorticity at 925 hPa was obtained. Using
190 these data and the automatic tracking scheme developed by Hodges (1994), cyclones at
191 925 hPa were identified in the study domain, which is the band between 75°S and 20°S
192 which extends eastward from 160°W to the Greenwich meridian. This band encompasses
193 highly populated areas of South America where the low-level extratropical cyclones
194 might have strong impacts. Cyclones with a minimum lifetime of 72 h were identified
195 when the relative vorticity was less than $-3.0 \times 10^{-5} \text{ s}^{-1}$. Cyclones within the grid box with
196 0.5° in latitude and longitude were counted. Cyclones that remain stationary in a grid box
197 were counted only once. This tracking method provides the trajectories of the cyclones.

198 In order to focus on the variable patterns associated with the cyclone occurrences,
199 for each grid point, we selected the time steps with cyclone occurrences within an area
200 with a 1000 Km ray from the grid point. This ray is in accordance with the typical
201 dimension of 2000 Km for a baroclinic wave (Orlanski 1975). Cyclones out of this area
202 were not considered for the time averages. Then, the variables were averaged over these
203 time steps during summer (December to February-DJF) and winter (June to August - JJA)
204 in the 1979-1993 and 2003-2017 periods. These averages were obtained for the short
205 wave kinetic energy, short wave available potential energy, baroclinic and barotropic
206 conversion terms.

207

208 **3. Results**

209

210 3.1. SST mean state

211

212 Figure 1 shows the summer and winter SST anomaly maps during the two selected
213 periods. The seasonal maps during the 2003-2017 period show dominantly positive
214 anomalies in the North Atlantic and negative ones in the 40-70°S band, and those during
215 the 1979-1993 period, reversed sign patterns, which are typical in the WAMO and
216 CAMO, respectively (Enfield and Mestas-Nuñez 1999; Folland et al. 1999; Mestas-
217 Nuñez and Enfield 2001; Enfield et al. 2001; Timmermann et al. 2007). These patterns
218 illustrate large-scale meridional SST anomalous gradients between the bands north and
219 south of 40°S, which are northward directed in the WAMO and southward directed in the
220 CAMO. In the Atlantic, the meridional SST anomalous gradient relates to thermohaline
221 circulation changes varying from decadal to multidecadal time scales (Kerr 2000;
222 Delworth and Mann 2000; Knight et al. 2006). Also, the PDO signature is apparent. The
223 negative SST anomalies in the central North Pacific and the positive ones in the eastern
224 tropical Pacific noted during both seasons in the 1979-1993 period are indicative of the
225 warm PDO (WPDO) phase, and the reversed sign anomaly patterns during both seasons
226 in the 2003-2017 period, of the cold PDO (CPDO) phase (Mantua et al., 1997; Zhang *et*
227 *al.*, 1997). Nevertheless, the anomalies in the eastern tropical Pacific are considerably
228 weak. in particular during the 2003-2017 period.

229 Therefore, both PDO phases might occur in this period. The annual AMO and
230 PDO indices during the 1979-2017 period are illustrated in Figure 2. The AMO index is
231 predominantly negative and the PDO index, positive, during the 1979-1993 period. While
232 the AMO index is predominantly positive during the 2003-2017 period, the PDO index
233 oscillates between positive (2003-2006 and 2014-2017 -WPDO) and negative (2008-

234 2013 -CPDO) values. Since the AMO remains in the same phase during the 2003-2017
235 period, if the PDO has a strong effect in the SST of the southern middle and high latitudes,
236 the SST patterns in these latitudes must present distinct features during the WPDO and
237 CPDO. However, the SST anomaly patterns in the middle and high latitudes during the
238 WPDO and CPDO do not show substantial differences (Fig. 3). Therefore, the SST
239 anomaly mean states presented in Figure 1 can be considered related to the AMO.

240 Therefore, the significant negative anomalies in the Drake Passage, southeastern
241 Pacific, and South Atlantic during both seasons in the 2003-2017 period are indeed part
242 of a large-scale WAMO-related SST anomaly pattern (Figs. 1a and 1c). The opposite sign
243 SST anomaly patterns during both seasons in the 1979-1993 period are related to the
244 CAMO (Figs. 1b and 1d). In general, the SST anomaly patterns feature nearly zonal
245 structures along the southern mid-latitudes, with strong meridional gradients in the South
246 Atlantic and southeastern Pacific. The east-west SST gradients are also apparent in some
247 cases, as between the Bellingshausen and Amundsen Seas during summer in the WAMO.
248 But the east-west SST gradients are less pronounced than the meridional gradients.
249 During both seasons, the northward SST anomalous gradient increases the baroclinicity
250 in the mid-latitudes in the WAMO; and the southward SST anomalous gradient decreases
251 the baroclinicity in these latitudes in the CAMO. Since this analysis refers to the low-
252 frequency SST variations, we can infer that the SST meridional gradients alter the long-
253 wave baroclinicity, which in turn takes part in the energy cycle. Therefore, the selected
254 periods show contrasting SST mean states under which the cyclones might present
255 distinct features. These differences are analyzed in the next subsections considering only
256 the time steps with the extratropical cyclone occurrences.

257

258 **3.2. Extra-tropical Cyclones**

259

260 The seasonal maps with the number of cyclones at 925 hPa per grid box in the
261 study domain are depicted in Figure 4. The cyclone trajectories vary seasonally and with
262 the AMO phases. During summer in the WAMO, the cyclone local counts exceeding 10
263 events per grid box occur mostly in the 50-60°S band between 150°W and 100°W, where
264 they turn southeastward along two preferred narrow bands, one of them extends across
265 the Drake Passage, and then to the South Atlantic in the 50-60°S band (Fig. 4a). Along
266 the high mid-latitudes, the number of grid boxes with cyclone local counts exceeding 10
267 events is lower in the South Atlantic than in the southeastern Pacific (Fig. 4a). Thus, the
268 cyclones in the southeastern Pacific might last longer or be slower than those crossing the
269 South Atlantic. One reason for the distinct behavior of the cyclones in these two oceanic
270 sectors is the SST background along the high mid-latitudes, which is anomalously more
271 negative in the Drake Passage and South Atlantic than in the southeastern Pacific (Fig.
272 1a).

273 During summer in the CAMO, the cyclone local counts exceeding 10 events
274 appear along narrow zonal areas in the 50-70°S band in the southeastern Pacific and along
275 the Drake Passage and in the 50-60°S band in the South Atlantic (Fig. 4b). In this case,
276 the largest cyclone local counts are channeled along the 50-70°S band, where positive
277 SST anomaly background prevails (Fig. 1b). During summer in the CAMO, the number
278 of grid boxes with cyclone local counts exceeding 10 events is higher than during summer
279 in the WAMO along the high mid-latitudes (Figs. 4a and 4b). This is due to the positive
280 summer SST anomaly mean state in these latitudes in the CAMO, and the negative one
281 in the WAMO (Figs. 1a, 4a, 1b and 4b).

282 During winter, the cyclone local counts exceeding 10 events per grid box are
283 spread in a larger latitudinal band mostly between 35°S and 75°S for both AMO phases

284 (Figs. 4c and 4d). During winter in the WAMO, the largest cyclone local counts exceeding
285 10 events per grid box occur along 40°S in the southeast Pacific and along 50°S in the
286 South Atlantic approximately over the regions with positive SST anomaly mean state
287 (Figs. 1c and 4c). In the case of winter in the CAMO the most prominent feature is the
288 maximum cyclone local counts along 68°S in the Bellingshausen Sea, which is a preferred
289 cyclolytic region (Simmonds and Keay 2000b) (Fig. 4d). So, a larger number of cyclones
290 remain in this region leading to the maximum cyclone local counts. This maximum is also
291 consistent with the positive SST anomaly mean state in the circumpolar and high middle
292 latitudes in the southeastern Pacific (Figs. 1d and 4d).

293 The cyclone densities in most latitudes during both seasons in the CAMO surpass
294 those in the WAMO (Fig. 5). Furthermore, the cyclone densities in most latitudes in both
295 AMO phases are higher during winter than during summer, except in the 50-57°S band.
296 This occurs due to the larger meridional temperature gradients during winter than during
297 summer (Figure not shown). During summer, the largest cyclone densities occur in the
298 50-60°S band, with a maximum of approximately 6 cyclones in the CAMO and 5.5
299 cyclones, in the WAMO (Fig. 5a). On the other hand, during winter, the cyclone densities
300 show several maxima, which reflect the largest counts per grid box along narrow zonal
301 bands (Figs. 4c, 4d and 5b). A winter maximum occurs around 68°S for both AMO
302 phases, which is the main peak with 8.5 cyclones per grid box in the CAMO, and the
303 secondary one with 4 cyclones per grid box in the WAMO. The winter graphs show other
304 peaks, around 60°S, 48°S and 42-40°S, which are consistent with the spatial distribution
305 of the cyclone counts (Figs. 4c, 4d and 5b).

306

307 **3.3. Available Potential and Kinetic Energies**

308

309 The summer and winter maps of the P_h and K_h in each AMO phase are illustrated
310 in Figures 6 and 7. The highest P_h values occur in the mid-latitudes with a maximum in
311 central northwestern Argentina during summer and in the low mid-latitudes and
312 subtropics during winter with a maximum in central Argentina and Uruguay, and the
313 lowest P_h values, in the southern extratropical latitudes (Fig. 6). These bands with the
314 largest P_h values are approximately 10° north of the corresponding oceanic high mid-
315 latitude bands with the largest cyclone local counts in the southeastern Pacific and
316 southwestern Atlantic (Figs. 4 and 6). During both seasons, the P_h values in the WAMO
317 exceed those in the CAMO over the study domain (Figure not shown). Thus, concerning
318 the available potential energy, this result indicates that the cyclones during both seasons
319 are more energetic in the WAMO than in the CAMO (Fig. 6).

320 In both AMO phases, the highest K_h values occur along the $30\text{-}50^\circ\text{S}$ and $20\text{-}50^\circ\text{S}$
321 bands, respectively during summer and winter, and the lowest ones, along the southern
322 high latitudes during both seasons (Fig. 7). The bands with the largest K_h are $10\text{-}20^\circ$ north
323 of the high mid-latitude bands with the largest cyclone local counts in the southeastern
324 Pacific and southwestern Atlantic (Figs. 4 and 7). Furthermore, the maximum K_h values
325 in the southwest Atlantic off the eastern coast of Argentina, Uruguay and southern Brazil
326 coincide with a previously documented cyclogenetic region (Sinclair 1995; 1997). During
327 both seasons, the K_h estimates in the study domain in the WAMO surpass those in the
328 CAMO. Thus, the considerably more energetic low-level cyclones in the study domain
329 might lead to higher energy conversion terms in the WAMO than in the CAMO.

330

331 **3.4. Baroclinic and Barotropic Energy conversion**

332

333 During both seasons in both AMO phases, significant positive $P_l P_h + P_h K_h$

334 (baroclinic conversion term) values are found in most of the study domain, except in
335 small areas of the subtropics (Fig. 8). The largest $P_l P_h + P_h K_h$ values during summer are
336 found in the 30-60°S band, and during winter in the 25-50°S band, in particular in the
337 southwestern Atlantic, where the largest P_h and K_h values are noted (Figs. 6, 7 and 8). The
338 southwestern Atlantic is a known cyclogenetic area (Sinclair 1995; 1997). The bands with
339 the largest $P_l P_h + P_h K_h$ are approximately 10° north of the corresponding mid-latitude
340 bands with the largest cyclone local counts in the southeastern Pacific and southwestern
341 Atlantic (Figs. 4 and 8). During both seasons, larger $P_l P_h + P_h K_h$ values occur in the
342 WAMO rather than in the CAMO. Thus, the cyclones are more baroclinic during the
343 WAMO. This result is consistent with the meridional SST anomalous gradients between
344 the bands north and south of the 40°S which are northward directed during the WAMO
345 and southward directed during the CAMO (Fig. 1). Thus, the SST mean state creates large
346 scale anomalous gradient favorable to increase the low-level cyclone baroclinity during
347 the WAMO in relation to the CAMO.

348 The maps of the barotropic conversion term of the Lorenz energy cycle ($K_l K_h$) are
349 depicted in Figure 9. The significant negative values of this energy conversion term, thus
350 reductions of the kinetic energy of the short waves and increases of the kinetic energy of
351 the long waves, are noted in most of the study domain south of 50°S during both seasons
352 and both AMO phases. This barotropic energy conversion is stronger in the WAMO than
353 in the CAMO. On the other hand, conversion of the K_l into K_h occurs in several bands,
354 whose location depends on the season and AMO phases. Positive $K_l K_h$ values are noted
355 in most of the band extending southeastward from the 30-40°S and 160-120°W area into
356 the central South Atlantic between 20° and the Greenwich longitudes and between 45°S
357 and 55°S during summer and between 50°S and 60°S during winter (Fig. 9). The positive
358 $K_l K_h$ values are not well defined during summer in the WAMO in the southeastern Pacific

359 (Fig. 9a). During winter in both AMO phases, another almost zonal band between 25°S
360 and 45°S and between 100°W and the Greenwich longitude is evident (Figs. 9c and 9d).
361 In this case, the barotropic conversion is stronger in the CAMO than in the WAMO.

362

363 **4. Discussions and conclusions**

364

365 This study investigated the hypothesis that the anomalous SST mean state
366 associated with the AMO might alter the low-level cyclone features in the southeastern
367 Pacific and South Atlantic using thirty nine years (1979-2017) of 6 hourly NCEP-DOE
368 Reanalysis-II (2018) (Kanamitsu et al. 2002) data. This period contains two periods of 15
369 years, which overlap the CAMO and WAMO phases, 1979-1993 and 2003-2017 periods,
370 respectively. In order to show that these periods represent the two AMO phases, we used
371 the monthly mean SST data from the extended reconstructed SST (NOAA/ERSST, 2018)
372 version V5 data for the 1870-2017 period (Huang *et al.*, 2015). In this case, we removed
373 the SST linear trends for the 1870-2017 period and the SST anomalies were based on the
374 1979-2017 base period. So, these anomalies do not contain the climate change trends.
375 Also, an automatic cyclone tracking algorithm was used to identify the 925 hPa cyclones
376 per grid box. We limited our study to the 20-75°S, 160-0°W area, whose southern portion
377 presents multi-decadal SST variability modulated by the AMO (Folland et al. 1999;
378 Timmermann et al. 2007).

379 The summer and winter SST anomaly maps during the 1979-1993 and 2003-2017
380 periods reproduced, respectively, the typical patterns previously documented in the
381 CAMO and WAMO phases (Enfield and Mestas-Nuñez 1999; Folland et al. 1999;
382 Mestas-Nuñez and Enfield 2001; Enfield et al. 2001; Timmermann et al. 2007). These
383 patterns show large-scale meridional SST anomalous gradients between the bands north

384 and south of 40°S, which are northward directed in the WAMO and southward directed
385 in the CAMO. The AMO-related large-scale SST anomaly patterns play an important role
386 in the cyclone trajectories and in the Lorenz energy cycle.

387 The positive SST anomalies of the mean state define approximately the cyclone
388 trajectories, which vary seasonally and with the AMO phases. Indeed, the number of grid
389 boxes with cyclone local counts exceeding 10 events during summer along the high mid-
390 latitudes is higher in the CAMO due to the positive SST anomalies in these latitudes
391 compared to negative ones in the WAMO (Figs. 1a, 4a, 1b and 4b). During winter in the
392 WAMO, the cyclone local counts exceeding 10 events per grid box along 40°S in the
393 southeast Pacific and along 50°S in the South Atlantic occur approximately in the areas
394 with positive SST anomalies (Figs. 1c and 4c). During winter in the CAMO the maximum
395 cyclone local counts along 68°S in the Bellingshausen Sea is driven by the positive SST
396 anomalies in the circumpolar and high middle latitudes in the southeastern Pacific (Figs.
397 1d and 4d). We also found that the cyclone densities in most latitudes during both seasons
398 are higher in the CAMO than in the WAMO (Fig. 5). Therefore, considering the 1979-
399 2017 period, the cyclone density in the study domain presents a reduction trend.
400 Consistently, Simmonds and Keay (2000a) documented a decrease trend in the annual
401 average number of cyclones in the 30-70°S band from 1970 to 1997.

402 The large-scale northward SST anomalous gradients between the bands north and
403 south of 40°S increase the baroclinicity in the mid-latitudes in the WAMO, and the
404 southward SST anomalous gradients decrease it in the CAMO. Our analysis refers to the
405 low-frequency SST variations, so the SST meridional gradients alter the long-wave
406 baroclinicity, which in turn takes part in the Lorenz energy cycle. Consistent with the
407 AMO-related increased long wave baroclinicity during both seasons, increased short
408 wave baroclinicity occurs in the WAMO compared to the CAMO (Fig. 8). Meanwhile, in

409 the South Atlantic region off the Argentinean coast, both the barotropic and baroclinic
410 conversion terms are positive indicating increase of the kinetic energy of the short waves
411 (Figs. 8 and 9). This is a known cyclogenetic region (Sinclair 1995; 1997).

412 Our results indicated higher cyclone densities in the CAMO than in the WAMO
413 in most latitudes during both seasons (Fig. 5). However, the cyclones are more energetic
414 during the WAMO than in the CAMO (Figs. 6-9). These distinct aspects of the low-level
415 cyclones in the southeastern Pacific and South Atlantic during the two AMO phases are
416 modulated by the AMO-related SST anomalies, with the positive anomalies affecting the
417 cyclone trajectories, and the meridional SST gradients, the baroclinicity of the long
418 waves, which in turn enters in the energy Lorenz cycle.

419 Although the linear trends were removed from the SST data, this procedure does
420 not completely remove the climate change signal. Nevertheless, the best estimate of the
421 natural component of the AMO is the removal of the model based estimates of the forced
422 component variability (Ting et al. 2009; Frankcombe et al. 2015; Frankignoul et al. 2017).
423 Since analysis with modeling outputs is out of the scope of the present study, we used
424 Frankignoul et al.'s (2017) results to support the hypothesis that the SST patterns during
425 the two selected periods contain the AMO signal. Their Figure 8 shows the mean AMO
426 pattern obtained after removing the anthropogenic effect from modeling estimates. Their
427 "true" AMO pattern shows opposite sign SST anomalies in the North Atlantic and the
428 southern middle and high latitudes. This pattern is similar to that shown in our Figure 1.
429 Thus, Figure 1 contains the AMO-related variability, which might be intensified due to
430 global change. However, this anthropogenic component does not invalidate our
431 conclusions.

432 Our analysis clearly illustrates the relations of the low-level extra-tropical
433 cyclones in the study domain to the AMO phases. As far as we know, these relations have

434 not been examined before. However, the cyclone related changes described here might
435 also be partially caused by the global warming between the two analyzed periods. The
436 results here might be relevant to future diagnostic and modeling studies on the SH low-
437 level extra-tropical cyclones. Finally, we are aware that the approach adopted here
438 considering two periods of 15 years as representative of the two AMO phases should be
439 validated with a longer period data. Such validation analysis is the subject of a future
440 study by the authors.

441

442 **5. Acknowledgements**

443

444 The Conselho Nacional de Desenvolvimento Científico e Tecnológico (CNPq) of
445 Brazil partially supported the first author under grant 302322/2017-5. The authors thank
446 the three anonymous reviewers for their useful comments and suggestions.

447

448 **References**

449 Befort, D. J., S. Wild, T. Kruschke, U. Ulbrich, and G. C. Leckebusch, 2016: Different
450 long-term trends of extra-tropical cyclones and windstorms in ERA-20C and
451 NOAA-20CR reanalyses. *Atmos. Sci. Lett.*, **17**, 586-595.

452 <https://doi.org/10.1002/asl.694>

453 Blackmon M. L., 1976: A climatological spectral study of the 500 mb geopotential height
454 of the Northern Hemisphere. *J. Atmos. Sci.*, **33**, 1607-1623.

455 [https://doi.org/10.1175/1520-0469\(1976\)033<1607:ACSSOT>2.0.CO;2](https://doi.org/10.1175/1520-0469(1976)033<1607:ACSSOT>2.0.CO;2)

456 Crowley, T. J., and K.-Y. Kim, 1993: Towards development of a strategy for determining
457 the origin of decadal-centennial scale climate variability. *Q. Sci. Rev.*, **12**, 375-385.

458 [https://doi.org/10.1016/S0277-3791\(05\)80003-4](https://doi.org/10.1016/S0277-3791(05)80003-4)

459 Delworth, T. L., and M. E. Mann, 2000: Observed and simulated multidecadal
460 variability in the Northern Hemisphere 2000. *Climate Dyn.*, **16**, 661–676.
461 <https://doi.org/10.1007/s003820000>

462 Eichler, T. P., and J. Gottschalck, 2013: A comparison of Southern Hemisphere cyclone
463 track climatology and interannual variability in coarse-gridded reanalysis datasets.
464 *Adv Meteor.*, **2013**, article ID 891260, 1-16.
465 <http://dx.doi.org/10.1155/2013/891260>

466 Enfield, D. B., and A. Mestas-Nuñez, 1999: Multiscale variabilities in global sea surface
467 temperatures and their relationships with tropospheric climate patterns. *J. Climate*,
468 **12**, 2719-2733. [https://doi.org/10.1175/1520-
469 0442\(1999\)012<2719:MVIGSS>2.0.CO;2](https://doi.org/10.1175/1520-0442(1999)012<2719:MVIGSS>2.0.CO;2)

470 Enfield, D. B., A. M. Mestas-Nuñez, and P. J. Trimble, 2001: The Atlantic multidecadal
471 oscillations and its relation to rainfall and river flows in the continental U.S.
472 *Geophys. Res. Lett.*, **28**, 2077–2080. <https://doi.org/10.1029/2000GL012745>

473 Folland, C. K., D. E. Parker, A. W. Colman, and R. Washington, 1999: Large-scale modes
474 of ocean surface temperature since the late nineteenth century. In: Navarra A (ed)
475 Beyond El Niño: decadal and interdecadal climate variability, first edn. Springer-
476 Verlag Berlin Heidelberg, Germany pp 73-102.

477 Frankcombe, L. M., M. H. England, M. E. Mann, and B. A. Steinman, 2015: Separating
478 internal variability from the externally forced climate response. *J. Climate*, **28**,
479 8184-8202. <https://doi.org/10.1175/JCLI-D-15-0069.1>

480 Frankignoul, C., G. Gastineau, and Y. O. Kwon, 2017: Estimation of the SST response to
481 anthropogenic and external forcing and its impact on the Atlantic Multidecadal
482 Oscillation and the Pacific Decadal Oscillation. *J. Climate*, **30**, 9871-9895.
483 <https://doi.org/10.1175/JCLI-D-17-0009.1>

484 Gan, M. A., and V. B. Rao, 1999: Energetics of the high frequency disturbances over
485 South America. *Rev. Bras .Geof.*, **17**, 21-28. [http://dx.doi.org/10.1590/S0102-](http://dx.doi.org/10.1590/S0102-261X1999000100003)
486 [261X1999000100003](http://dx.doi.org/10.1590/S0102-261X1999000100003)

487 Goldenberg, S. B., C. W. Landsea, A. M. Mestas-Nuñez, and W. M. Gray, 2001: The
488 recent increase in Atlantic hurricane activity: causes and implications. *Science*, **293**,
489 474–479. <https://doi.org/10.1126/science.1060040>

490 Gómara, I., B. Rodríguez-Fonseca, P. Zurita-Gotor, S. Ulbrich, and J. G. Pinto, 2016:
491 Abrupt transitions in the NAO control of explosive North Atlantic cyclone
492 development. *Climate Dyn.*, **47**, 3091–3111. [https://doi.org/10.1007/s00382-016-](https://doi.org/10.1007/s00382-016-3015-9)
493 [3015-9](https://doi.org/10.1007/s00382-016-3015-9)

494 Grieger, J., G. C. Leckebusch, C. C. Raible, I. Rudeva, and I. Simmonds, 2018:
495 Subantarctic cyclones identified by 14 tracking methods, and their role for moisture
496 transports into the continent. *Tellus A: Dynamic Meteorology and Oceanography*,
497 **70**, 1454808, 1-18. <https://doi.org/10.1080/16000870.2018.1454808>

498 Hodges, K. I. 1994: A general-method for tracking analysis and its application to
499 meteorological data. *Mon. Wea. Rev.*, **122**, 2573-2586. [https://doi:10.1175/1520-](https://doi:10.1175/1520-0493(1994)122<2573:AGMFTA>2.0.CO;2)
500 [0493\(1994\)122<2573:AGMFTA>2.0.CO;2](https://doi:10.1175/1520-0493(1994)122<2573:AGMFTA>2.0.CO;2)

501 Huang, B., and Coauthors, 2015: Extended reconstructed sea surface temperature version
502 4 (ERSST.v4). Part I: Upgrades and intercomparisons. *J. Climate*, **28**: 911–930.
503 <https://doi.org/10.1175/JCLI-D-14-00006.1>

504 JISAO/PDO (Joint Institute for the Study of the Atmosphere and Ocean/Pacific Decadal
505 Oscillation) PDO index time series. 2019. Access: March 25, 2019.
506 <http://research.jisao.washington.edu/pdo/>

507 Jones, D. A., and I. Simmonds, 1993: Climatology of Southern Hemisphere extratropical
508 cyclones. *Climate Dyn.*, **9**, 131-145. <https://doi.org/10.1007/BF00209750>

509 Kanamitsu, M., W. Ebisuzaki, J. Woollen, S.-K. Yang, J. J. Hnilo, M. Fiorino, and G. L.
510 Potter, 2002: NCEP–DOE AMIP-II Reanalysis (R-2). *Bull. Amer. Meteor. Soc.*, **83**,
511 1631-1643. <https://doi.org/10.1175/BAMS-83-11-1631>

512 Kerr, R. A. 2000: A North Atlantic climate pacemaker for the centuries. *Science*, **288**,
513 1984–1986. <https://doi.org/10.1126/science.288.5473.1984>

514 Knight, J. R., C. K. Folland, and A. A. Scaife, 2006: Climate impacts of the Atlantic
515 multidecadal oscillation. *Geophys. Res. Lett.* **33**, L17706.
516 <https://doi.org/10.1029/2006GL026242>

517 Mantua, N. J., S.R. Hare, Y. Zhang, J. M. Wallace, and R. C. Francis, 1997: A Pacific
518 interdecadal climate oscillation with impacts on salmon production. *Bull. Amer.*
519 *Meteor. Soc.*, **78**, 1069-1079. [https://doi.org/10.1175/1520-0477\(1997\)078<1069:APICOW>2.0.CO;2](https://doi.org/10.1175/1520-0477(1997)078<1069:APICOW>2.0.CO;2)

521 Mendes, D., E. P. Souza, J. A. Marengo, and M. C. D. Mendes 2009: Climatology of
522 extratropical cyclones over the South American–southern oceans sector *Theor.*
523 *Appl. Climatol.*, **100**, 239-250. <https://doi.org/10.1007/s00704-009-0161-6>

524 Mestas-Nuñez, A. M., and D. B. Enfield, 2001: Eastern equatorial Pacific SST variability:
525 ENSO and non-ENSO components and their climate associations. *J. Climate*, **14**,
526 391-402. [https://doi.org/10.1175/1520-0442\(2001\)014<0391:EEPSVE>2.0.CO;2](https://doi.org/10.1175/1520-0442(2001)014<0391:EEPSVE>2.0.CO;2)

527 NCEP-DOE Reanalysis-II (National Centers for Environmental Prediction - Department
528 of Energy Reanalysis-II) dataset. 2018. Access: from April 18, 2018 to May 05
529 2018. <https://www.esrl.noaa.gov/psd/data/gridded/>

530 Neu, U., and coauthors, 2013: IMILAST - a community effort to intercompare
531 extratropical cyclone detection and tracking algorithms. *Bull. Amer. Meteor. Soc.*,
532 **94**, 529-547. <https://doi.org/10.1175/BAMS-D-11-00154.1>

533

534 NOAA/AMO (National Oceanic and Atmospheric Administration/Atlantic Multidecadal
535 Oscillation) AMO index time series. 2019. Access: March 25, 2019.
536 <https://www.esrl.noaa.gov/psd/data/timeseries/AMO/>

537 NOAA/ERSST (National Oceanic and Atmospheric Administration/Extended
538 Reconstructed Sea Surface Temperature) SST data. 2018. Access: December 6,
539 2018. <https://www.esrl.noaa.gov/psd/data/gridded/>

540 Orlandi, I., 1975: A rational subdivision of scales for atmospheric processes. *Bull. Amer.*
541 *Meteor. Soc.*, **56**, 527-530.
542 <https://journals.ametsoc.org/doi/pdf/10.1175/1520-0477-56.5.527>

543 Orlandi, I., and J. Katzfey, 1991: The life cycle of a cyclone wave in the Southern
544 Hemisphere. Part I: eddy energy budget. *J. Atmos. Sci.*, **48**, 1972-1998.
545 [https://doi.org/10.1175/1520-0469\(1991\)048<1972:TLCOAC>2.0.CO;2](https://doi.org/10.1175/1520-0469(1991)048<1972:TLCOAC>2.0.CO;2)

546 Parker, D. E., P. D. Jones, C. K. Folland, and A. Bevan, 1994: Interdecadal changes of
547 surface temperature since the late nineteenth century. *J. Geophys. Res.*, **99**, 14373–
548 14399. <https://doi.org/10.1029/94JD00548>

549 Peixoto, J. P., and A. H. Oort, 1992: Physics of climate. San Diego, CA, USA: MIT
550 press.

551 Pinto, J. R. D., and R. P. Rocha, 2011: The energy cycle and structural evolution of
552 cyclones over southeastern South America in three case studies. *J. Geophys. Res.*,
553 **116**, D14112. <https://doi:10.1029/2011JD016217>

554 Reason, C. J. C. 2000: Multidecadal climate variability in the subtropics: mid-latitudes of
555 the Southern Hemisphere oceans. *Tellus*, **52A**, 204–223.
556 <https://doi.org/10.1034/j.1600-0870.2000.00978.x>

557 Reason, C. J. C., and R. J. Murray, 2001: Modelling low frequency variability in southern
558 hemisphere extra-tropical cyclone characteristics and its sensitivity to sea-surface
559 temperature. *Int. J. Climatol.*, **21**, 249-267. <https://doi.org/10.1002/joc.608>

560 Reboita, M. S., R. P. Rocha, T. Ambrizzi, and C. D. Gouveia, 2015: Trend and
561 teleconnection patterns in the climatology of extratropical cyclones over the
562 Southern Hemisphere. *Climate Dyn.*, **45**, 1929–1944.
563 <https://doi.org/10.1007/s00382-014-2447-3>

564 Rosa, M. B., N. J. Ferreira, M. A. Gan, and L. H. R. Machado, 2013: Energetics of
565 cyclogenesis events over the southern coast of Brazil. *Rev. Bras. Meteor.*, **28**, 231-
566 245. <http://dx.doi.org/10.1590/S0102-77862013000300001>

567 Schlesinger, M. E., and N. Ramankutty, 1994: An oscillation in the global climate
568 system of period 65–70 years. *Nature*, **367**, 723-726.
569 <https://doi.org/10.1038/367723a0>

570 Schneider, D. P. and R. L. Fogt, 2018: Artifacts in century-length atmospheric and
571 coupled Reanalyses over Antarctica due to historical data availability. *Geophys.*
572 *Res. Lett.* **45**: 964-973. <https://doi.org/10.1002/2017GL076226>

573 Simmonds, I., and K. Keay, 2000a: Variability of southern hemisphere extratropical
574 cyclone behavior, 1958-97. *J. Climate*, **13**, 550-561.

575 Simmonds, I., and K. Keay, 2000b: Mean Southern Hemisphere extratropical cyclone
576 behavior in the 40-year NCEP–NCAR reanalysis. *J. Climate*, **13**, 873–885.
577 [https://doi.org/10.1175/1520-0442\(2000\)013<0873:MSHECB>2.0.CO;2](https://doi.org/10.1175/1520-0442(2000)013<0873:MSHECB>2.0.CO;2)

578 Sinclair, M. R., 1994: An objective cyclone climatology for the Southern Hemisphere.
579 *Mon. Wea. Rev.*, **122**, 2239–2256. [https://doi.org/10.1175/1520-0493\(1994\)122<2239:AOCCT>2.0.CO;2](https://doi.org/10.1175/1520-0493(1994)122<2239:AOCCT>2.0.CO;2)

580

581 Sinclair, M. R., 1995: A climatology of cyclogenesis for the Southern Hemisphere. *Mon.*
582 *Wea. Rev.*, **123**, 1601–1619. [https://doi.org/10.1175/1520-](https://doi.org/10.1175/1520-0493(1995)123<1601:ACOCFT>2.0.CO;2)
583 [0493\(1995\)123<1601:ACOCFT>2.0.CO;2](https://doi.org/10.1175/1520-0493(1995)123<1601:ACOCFT>2.0.CO;2)

584 Sinclair, M. R., 1997: Objective identification of cyclones and their circulation intensity,
585 and climatology. *Wea. Forecasting*, **12**, 595–612. [https://doi.org/10.1175/1520-](https://doi.org/10.1175/1520-0434(1997)012<0595:OIOCAT>2.0.CO;2)
586 [0434\(1997\)012<0595:OIOCAT>2.0.CO;2](https://doi.org/10.1175/1520-0434(1997)012<0595:OIOCAT>2.0.CO;2)

587 Timmermann, A., and Coauthors, 2007: The influence of a weakening of the Atlantic
588 meridional overturning circulation on ENSO. *J. Climate*, **20**, 4899–4919.
589 <https://doi.org/10.1175/JCLI4283.1>

590 Ting, M., Y. Kushnir, R. Seager, and C. Li, 2009: Forced and internal Twentieth-Century
591 SST trends in the North Atlantic. *J. Climate*, **22**, 1469–1481.
592 <https://doi.org/10.1175/2008JCLI2561.1>

593 Varino, F., P. Arbogast, B. Joly, G. Riviere, M.-L. Fandeur, H. Bovy, and J.-B. Granier,
594 2018: Northern Hemisphere extratropical winter cyclones variability over the 20th
595 century derived from ERA-20C reanalysis. *Climate Dyn.*, (published on line March
596 2018). <https://doi.org/10.1007/s00382-018-4176-5>

597 Venegas, S. A., L. A. Mysak, and D. N. Straub, 1996: Evidence for interannual and
598 interdecadal climate variability in the South Atlantic. *Geophys. Res. Lett.*, **23**, 2673–
599 2676. <https://doi.org/10.1029/96GL02373>

600 Venegas, S. A., L. A. Mysak, and D. N. Straub, 1998: An interdecadal climate cycle in
601 the South Atlantic and its links to other ocean basins. *J. Geophys. Res.*, **103**, 24723–
602 24736. <https://doi.org/10.1029/98JC02443>

603 Wang, X. L., Y. Feng, G. P. Compo, V. R. Swail, F. W. Zwiers, R. J. Allan, and
604 P. D. Sardeshmukh, 2013: Trends and low frequency variability of extratropical

605 cyclone activity in the ensemble of twentieth century reanalysis. *Climate Dyn.*, **40**,
606 2775–2800. <https://doi.org/10.1007/s00382-012-1450-9>
607 Zhang, Y., J. M. Wallace, and D. Battisti, 1997: ENSO-like interdecadal variability:
608 1900-93. *J. Clim.*, **10**, 1004-1020.
609 [https://doi.org/10.1175/1520-0442\(1997\)010<1004:ELIV>2.0.CO;2](https://doi.org/10.1175/1520-0442(1997)010<1004:ELIV>2.0.CO;2)
610

611 Figure Captions

612

613 Fig. 1 – Seasonal SST anomaly patterns during summer in the: (a) WAMO; (b) CAMO
614 and during winter in the: c) WAMO; d) CAMO. Shades interval is in °C indicated
615 by color bar. The continuous (dashed) line encompasses positive (negative)
616 significant values at the 95% confidence level using the Student's t-test. The zero
617 line was omitted.

618 Fig. 2 – Annual PDO and AMO indices during the 1979-2017 period. Positive PDO index
619 values are red, and the negative ones, blue. The AMO index is the black continuous
620 lines.

621 Fig. 3. Seasonal SST anomaly patterns during summer in the: (a) WAMO/WPDO; (b)
622 WAMO/CPDO and during winter in the: c) WAMO/WPDO; d) WAMO/CPDO.
623 Display is the same as in Figure 1.

624 Fig. 4 – Number of the 925 hPa cyclones during summer in the: (a) WAMO; (b) CAMO
625 and during winter in the: (c) WAMO; (d) CAMO.

626 Fig. 5 – Density of 925 hPa cyclones in the longitudinal band between 160°W and the
627 Greenwich Meridian during: (a) summer; (b) winter. Open and closed circles refer
628 to the CAMO and WAMO phases, respectively.

629 Fig. 6 – Available potential energy patterns during summer in the: (a) WAMO; (b)
630 CAMO and during winter in the: c) WAMO; d) CAMO. Shades interval is in $1e^{-1}$
631 KJ s^{-2} indicated by color bar.

632 Fig. 7 – Kinetic energy patterns during summer in the: (a) WAMO; (b) CAMO and during
633 winter in the: c) WAMO; d) CAMO. Shades interval is in $1e^{-1}$ KJ s^{-2} indicated by
634 color bar.

635 Fig. 8 - Baroclinic conversion of energy during summer in the: (a) WAMO; (b) CAMO
636 and during winter in the: c) WAMO; d) CAMO. Shades interval is in $W s^{-2}$
637 indicated by color bar. The continuous (dashed) line encompasses positive
638 (negative) significant values at the 95% confidence level using the Student's t-
639 test.

640 Fig. 9 – Barotropic conversion of energy during summer in the: (a) WAMO; (b) CAMO
641 and during winter in the: c) WAMO; d) CAMO. Shades interval is in $W s^{-2}$
642 indicated by color bar. The continuous (dashed) line encompasses positive
643 (negative) significant values at the 95% confidence level using the Student's t-test.

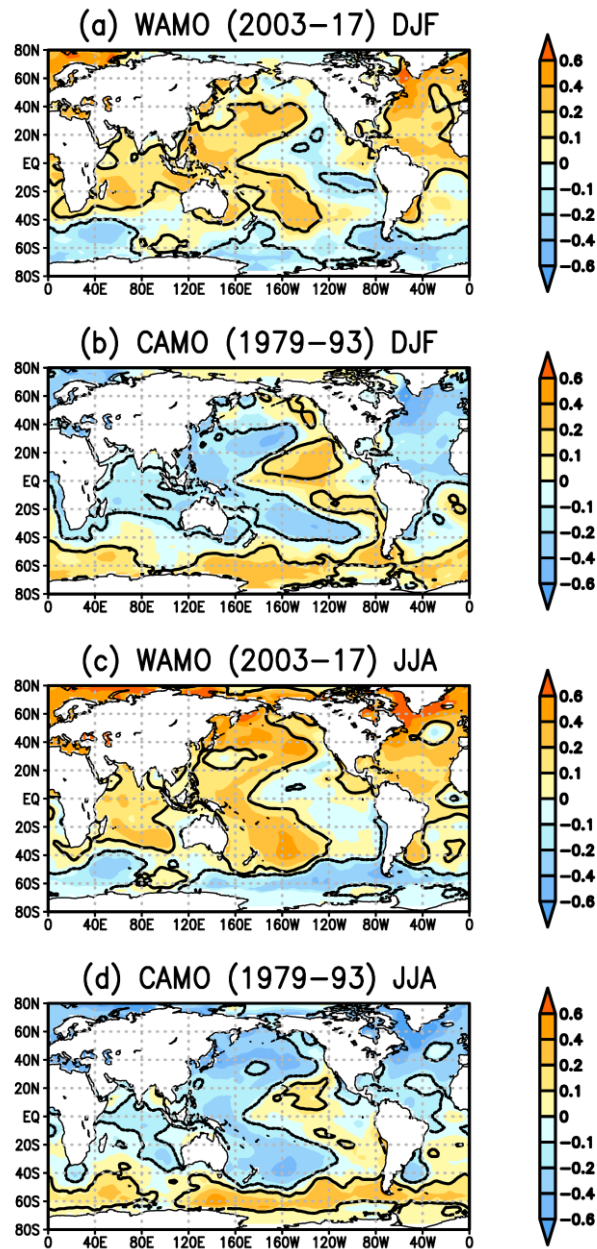


Fig. 1 – Seasonal SST anomaly patterns during summer in the: (a) WAMO; (b) CAMO and during winter in the: (c) WAMO; (d) CAMO. Shades interval is in °C indicated by color bar. The continuous (dashed) line encompasses positive (negative) significant values at the 95% confidence level using the Student’s t-test. The zero line was omitted.

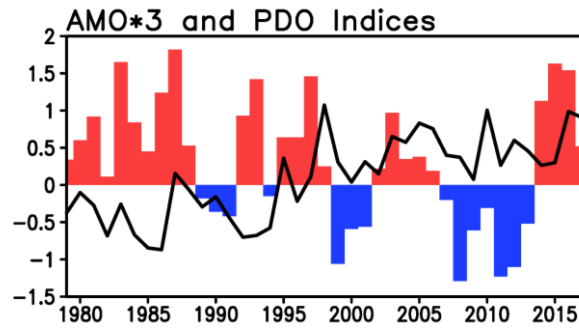


Fig. 2 – Annual PDO and AMO indices during the 1979-2017 period. Positive PDO index values are red, and the negative ones, blue. The AMO index is the black continuous lines.

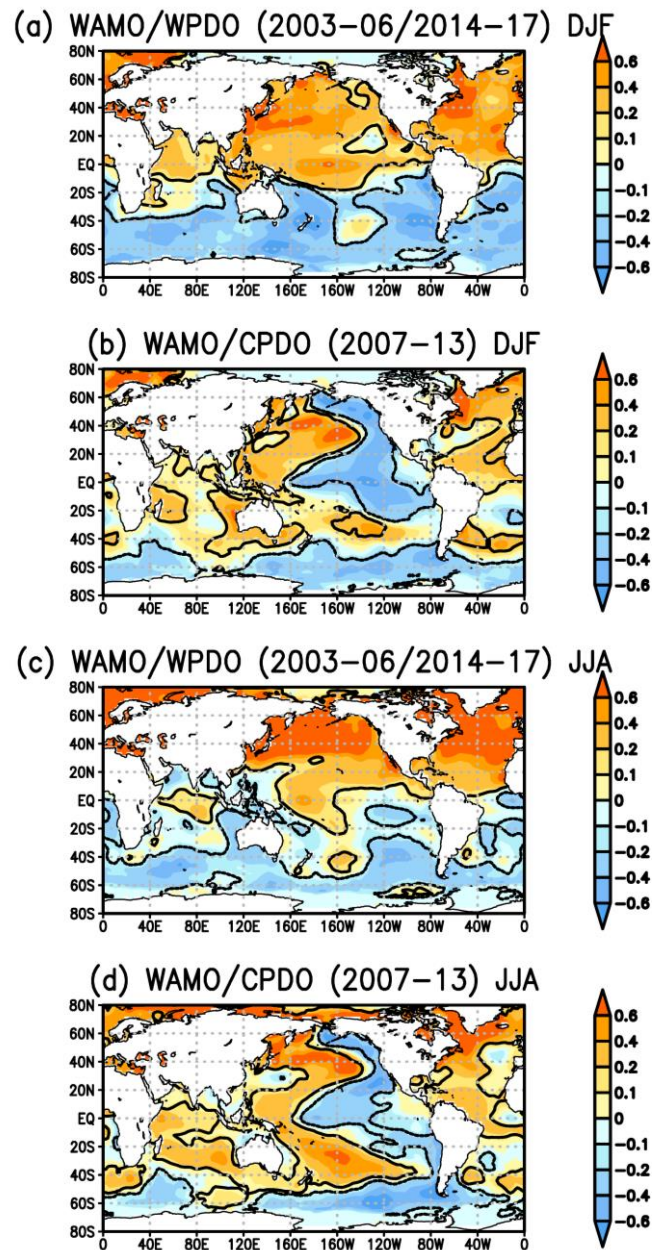


Fig. 3. Seasonal SST anomaly patterns during summer in the: (a) WAMO/WPDO; (b) WAMO/CPDO and during winter in the: (c) WAMO/WPDO; (d) WAMO/CPDO.

Display is the same as in Figure 1.

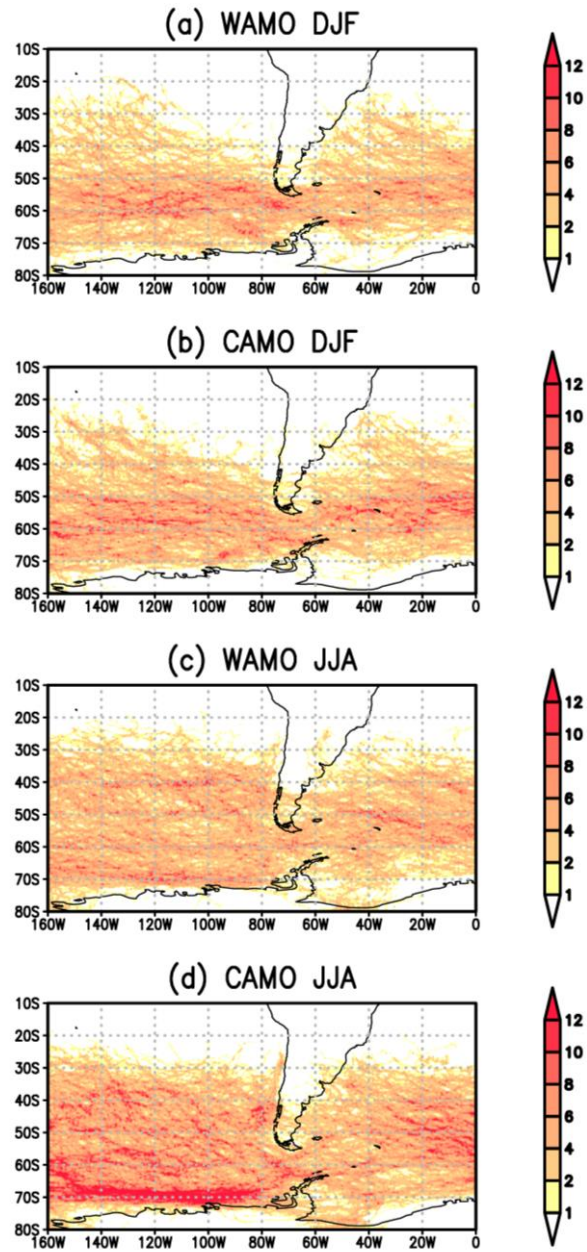


Fig. 4 – Number of the 925 hPa cyclones during summer in the: (a) WAMO; (b) CAMO and during winter in the: (c) WAMO; (d) CAMO.

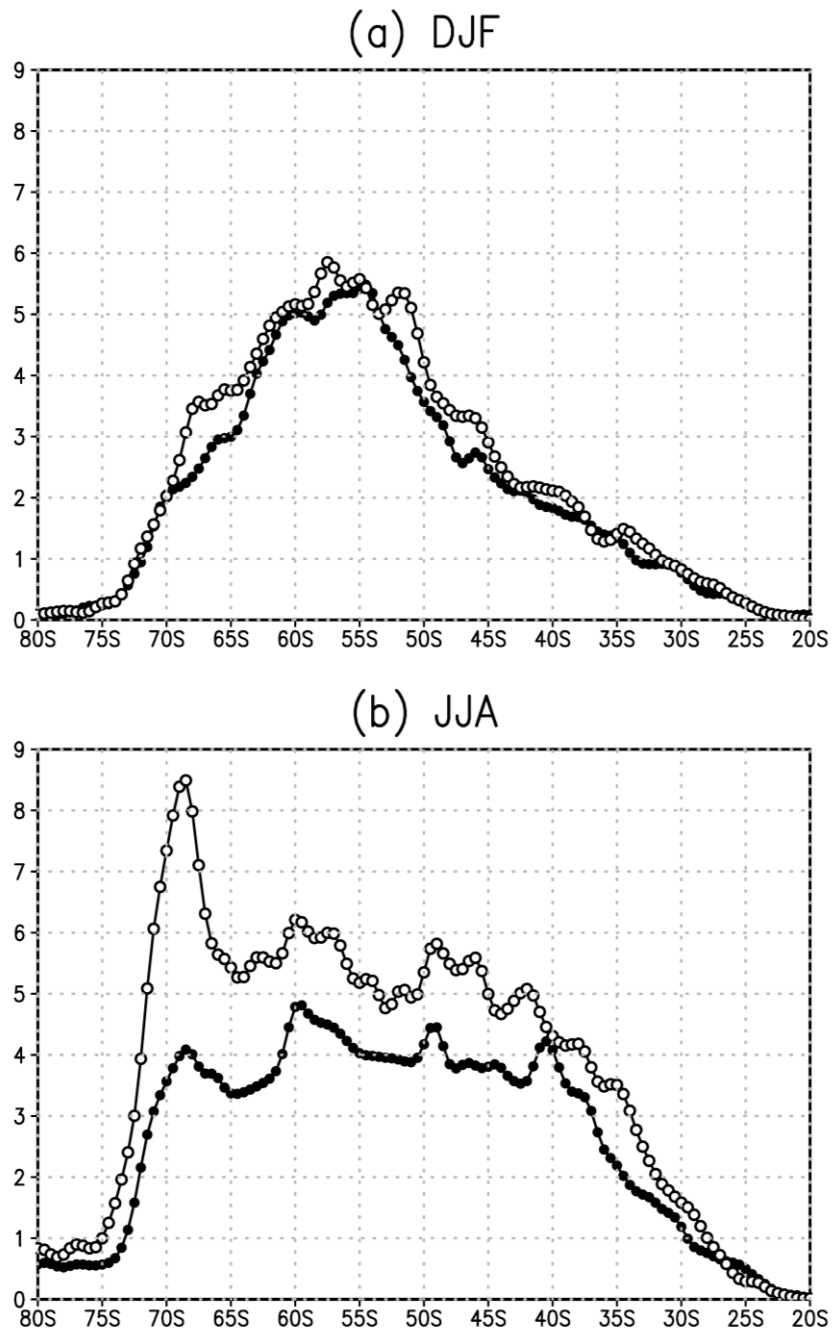


Fig. 5 – Density of 925 hPa cyclones in the longitudinal band between 160°W and the Greenwich Meridian during: (a) summer; (b) winter. Open and closed circles refer to the CAMO and WAMO phases, respectively.

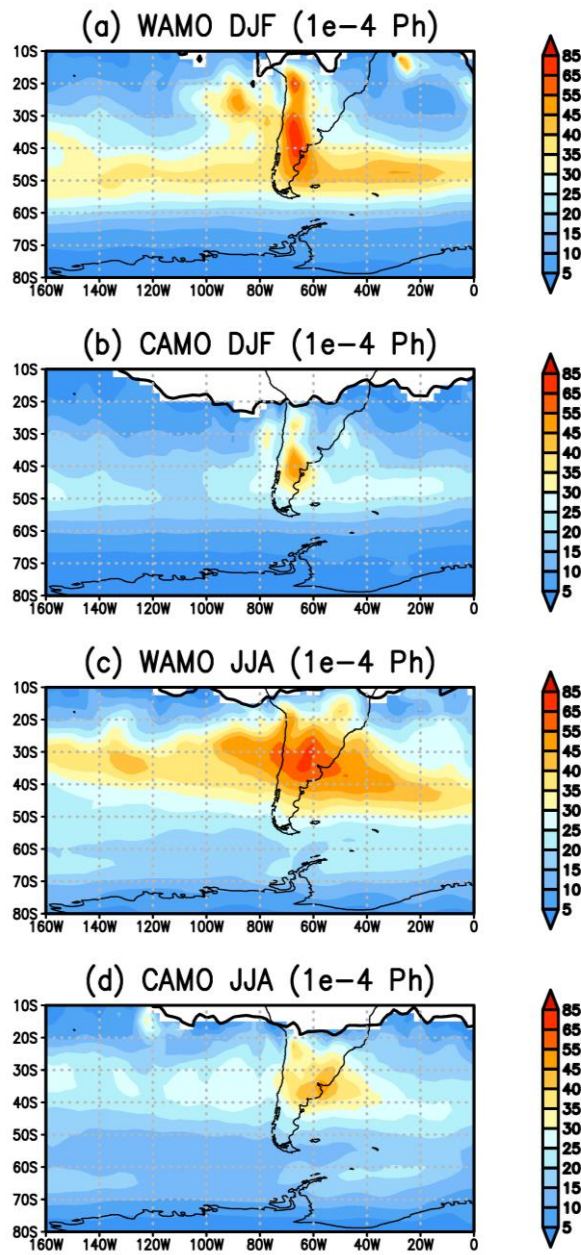


Fig. 6 – Available potential energy patterns during summer in the: (a) WAMO; (b) CAMO and during winter in the: c) WAMO; d) CAMO. Shades interval is in $1e^{-4}$ KJ s^{-2} indicated by color bar.

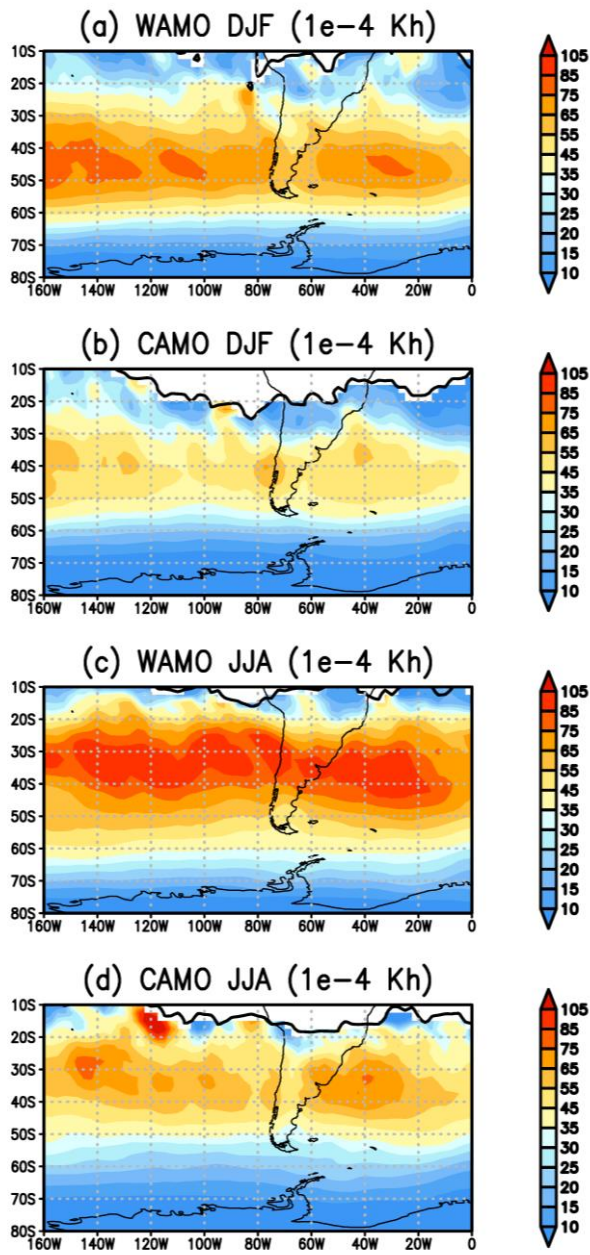


Fig. 7 – Kinetic energy patterns during summer in the: (a) WAMO; (b) CAMO and during winter in the: (c) WAMO; (d) CAMO. Shades interval is in $10^{-1} \text{ KJ s}^{-2}$ indicated by color bar.

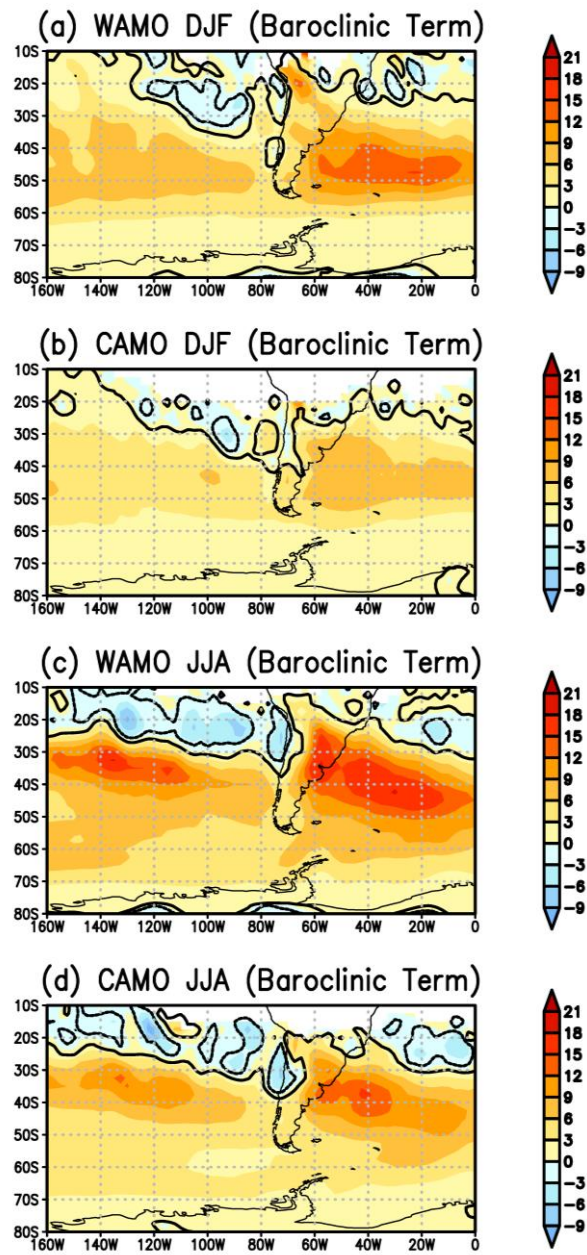


Fig. 8 - Baroclinic conversion of energy during summer in the: (a) WAMO; (b) CAMO and during winter in the: c) WAMO; d) CAMO. Shades interval is in $W s^{-2}$ indicated by color bar. The continuous (dashed) line encompasses positive (negative) significant values at the 95% confidence level using the Student's t-test.

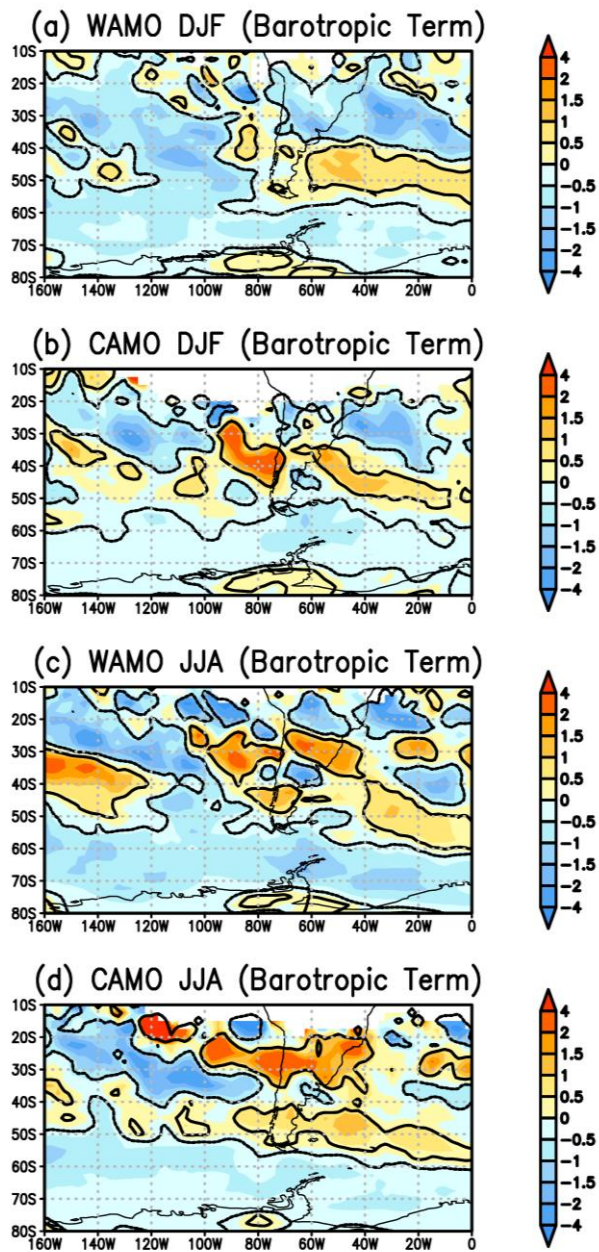


Fig. 9 – Barotropic conversion of energy during summer in the: (a) WAMO; (b) CAMO and during winter in the: (c) WAMO; (d) CAMO. Shades interval is in $W s^{-2}$ indicated by color bar. The continuous (dashed) line encompasses positive (negative) significant values at the 95% confidence level using the Student's t-test.